Analyst

ROYAL SOCIETY OF CHEMISTRY

Check for updates

MIL-68(In)-derived CdIn$_2$S$_4$@In$_2$S$_3$ hollow microtubes for a sensitive molecularly imprinted photoelectrochemical CEA sensor

Yang Zang, [iD] * Ruhua Wei, Yang Feng, Jingjing Jiang [iD] * and Huaiguo Xue

Herein, an antibody-free photoelectrochemical sensing platform was constructed for a sensitive carcinoembryonic antigen (CEA) assay by coupling CdIn$_2$S$_4$@In$_2$S$_3$ hollow microtubes (HMTs) and a polydopamine-mediated molecularly imprinted polymer (MIP). The CdIn$_2$S$_4$@In$_2$S$_3$ HMTs, synthesized by a Cd^{2+}-exchange reaction on an MIL-68(In)-derived In$_2$S$_3$ surface with a large specific surface area, could promote the separation of photogenerated charge carriers by shortening the charge-transfer distance and enhancing light absorption, resulting in a stable photocurrent. Furthermore, the polydopamine-dependent MIP, electrodeposited on the surface of a CdIn$_2$S$_4$@In$_2$S$_3$ HMTs-modified ITO electrode, could elute the template molecules to effectively recognize CEA without complex and expensive antibody–antigen assembly processes. In the presence of the target, CEA, the imprinted cavities could be re-embedded for inhibiting the diffusion of the electron donor *via* a typical steric-hindrance effect. Under optimized conditions, the developed sensor exhibited a wide linear range of 1 pg mL^{-1}–500 ng mL^{-1}, a low detection limit of 0.52 pg mL^{-1}, high selectivity and good stability. This sensor was also applied to the CEA analysis of real human serum, providing a feasible strategy for the selective detection of other biomarkers.

Introduction

Carcinoembryonic antigen (CEA), an acidic glycoprotein found in adult cancer tissues and fetal gastrointestinal epithelial tissues, usually serves as a common disease biomarker for colorectal cancer, breast cancer, and lung cancer.[1–3] The concentration of CEA in healthy adult blood serum is no more than 5 ng mL^{-1}, and an abnormal CEA level has been regarded as a warning sign for potential cancer risk.[4,5] Thus, the sensitive and selective detection of trace CEA holds great significance for screening high-risk cancers. Nowadays, several sensing techniques have been developed for CEA monitoring, such as electrochemical, electrochemiluminescence, fluorescence and enzyme-linked immunosorbent assays.[6–9] As a powerful analytical technique, photoelectrochemical (PEC) sensors have garnered widespread attention due to their high sensitivity, low detection cost and small background signal, which can effectively avoid the use of expensive instruments and complex operating procedures.[10–12] Considering the important role of the detection platform, a variety of semiconductor materials have been exploited with the capability of facilitating efficient signal conversion from excitation light to a detectable current, ensuring the sensitivity of PEC sensors.

Indium sulfide (In$_2$S$_3$), an n-type semiconductor with an appropriate band gap (1.9–2.4 eV), exhibits efficient visible-light absorption and desirable stability.[13–15] However, the application of pure In$_2$S$_3$ is limited by the rapid recombination of photoinduced charge carriers and severe photocorrosion. To address the above problems, it is feasible to construct an In$_2$S$_3$-based heterostructure using other semiconductors with a matched energy level.[16,17] For example, a hollow TiO$_2$@In$_2$S$_3$ photocatalyst rich in surface oxygen vacancies was synthesized, in which the obtained hollow cavities, heterostructure and oxygen vacancies were conducive to the separation of photogenerated charge carriers, light harvesting and CO$_2$ adsorption, respectively, resulting in excellent photocatalytic activity and durability for CO$_2$ reduction.[18] In particular, CdIn$_2$S$_4$, as a promising ternary metal, has aroused widespread interest due to its structural stability and suitable bandgap for visible-light absorption.[19,20] Additionally, numerous studies on CdIn$_2$S$_4$-based heterostructures have demonstrated impressive photoelectrochemical sensing and photocatalytic properties under visible-light irradiation.[21–23] For instance, a dual-mode fluorescent and PEC sensor was designed for the sensitive monitoring of 17β-estradiol with the aid of magnetic bead-assisted extraction, demonstrating PEC and fluorescent signals. Additionally, hollow CdIn$_2$S$_4$ microspheres were prepared as a promising photoactive matrix with enhanced photoelectrochemical signal and detection stability.[24]

Moreover, molecularly imprinted polymers (MIP) have great superiority in reinforcing the selectivity of PEC sensors. When

School of Chemistry and Chemical Engineering, Yangzhou University, Yangzhou, Jiangsu, 225002, P. R. China. E-mail: zangyang@yzu.edu.cn, jjj@yzu.edu.cn

template molecules are eluted from MIP, the blotting cavities can effectively capture target molecules with their matched molecular configuration by means of the high affinity between the imprinted cavities and target.[25,26] For example, a novel CEA-imprinted hydrogel membrane was immobilized on the surface of a gold nanoball/MoSe₂ nanosheet/glassy carbon electrode by using BCCPEimBr ionic liquid as a functional monomer; further development led to a selective PEC sensor for CEA detection with a low detection limit of 11.2 pg mL⁻¹.[27] Since protein blotting is usually performed in aqueous solution at room temperature, the selection of functional monomers plays an important role in the recognition and stability of MIP. Among these functional monomers, polydopamine (PDA)-based MIP, which consists of abundant catechol structures and amine groups, can improve protein imprinting efficiency through typical noncovalent interactions (*e.g.*, hydrogen bonding and π–π interaction) accompanied by good dispersion and biocompatibility.[28,29] Based on the synergistic effect of the heterostructured semiconductor hybrid and MIP, the designed PEC sensor can effectively avoid the expensive biological reagents/probes and the complex antibody–antigen assembly processes, which are beneficial for achieving a low detection cost and high selectivity.

In this work, $CdIn_2S_4@In_2S_3$ hollow microtubes (HMTs) were prepared by hydrothermal and ion-exchange methods, and an enhanced photocurrent response was achieved due to appropriate band matching between $CdIn_2S_4$ and In_2S_3. By using CEA as a template molecule and dopamine (DA) as a functional monomer, PDA-MIP was immobilized on the surface of the $CdIn_2S_4@In_2S_3$-modified ITO electrode by electropolymerization, and then a novel antibody-free, molecularly imprinted photoelectrochemical (MIP-PEC) sensing platform was constructed for the CEA assay after the removal of the template molecules (Scheme 1). In the presence of the target, CEA, abundant imprinted cavities with specific recognition sites could be re-occupied, blocking the diffusion of the electron donor (ascorbic acid, AA) from the electrolyte to

$CdIn_2S_4@In_2S_3$ HMTs, resulting in a decreased photocurrent. By virtue of the desirable recognition ability of PDA-MIP and the high photoelectric conversion efficiency of the $CdIn_2S_4@In_2S_3$ HMTs, the above MIP-PEC sensor has excellent properties for the CEA assay, and no additional immunoreaction is required for signal regulation.

Experimental

Preparation of In_2S_3 HMTs and $CdIn_2S_4@In_2S_3$/ITO

The MIL-68(In)-derived In_2S_3 HMTs were prepared by a previously reported method.[30] Firstly, 0.6 g 1,4-terephthalic acid and 0.8 g indium nitrate tetrahydrate were mixed into 40 mL of DMF and stirred for 5 min, and the resulting mixture was reacted at 120 °C for 30 min, followed by cooling to room temperature. The white precipitate was then washed with deionized water and ethanol several times, and the MIL-68(In) precursor was achieved after being dried at 60 °C for 12 h.

Additionally, the as-prepared MIL-68(In) was dissolved in 40 mL of ethanol solution containing 0.2 g thiourea. After ultrasonic stirring for 5 min, the above mixture was transferred into a 100 mL Teflon-lined, stainless-steel autoclave, and heated at 180 °C for 3 h. The obtained yellow precipitate was washed with deionized water, then washed thrice with ethanol, and dried in 60 °C for 12 h in sequence, and In_2S_3 HMTs were obtained for use in the subsequent experiments.

Prior to the preparation of the photoanodes, the ITO electrodes were cleaned with 1.0 M NaOH solution, 10% H_2O_2, ethanol and deionized water for 30 min, respectively, then dried under nitrogen. Thereafter, 10 µL of 3 mg mL⁻¹ In_2S_3 was dripped onto the pretreated ITO surface, and the In_2S_3/ITO electrode was obtained after drying at room temperature. Similarly, 10 µL of 0.1 M $Cd(NO_3)_2$ was coated onto the In_2S_3/ITO electrode, accompanied by an *in situ* Cd^{2+} exchange reaction at 60 °C for 10 min. The above photoanode was slowly rinsed with phosphate-buffered saline (PBS) to eliminate excess salt solution on the electrode surface, which was then dried at room temperature (denoted as $CdIn_2S_4@In_2S_3$/ITO).

Fabrication of MIP- and nonimprinted polymer (NIP)-modified $CdIn_2S_4@In_2S_3$/ITO

The MIP-based sensing platform was constructed as follows: firstly, 4 mL of 0.1 M PBS at pH 7.4 containing 5 mM DA and 0.5 µg mL⁻¹ CEA was purged with N₂ for 20 min to remove the dissolved oxygen. When the $CdIn_2S_4@In_2S_3$/ITO electrode was soaked in the above reaction mixture, the cyclic voltammetry experiment was then performed for 20 cycles in the potential range of −0.5 V to 0.5 V (scanning rate: 0.02 V s⁻¹). Finally, MIP/$CdIn_2S_4@In_2S_3$/ITO was immersed in 0.1 M NaOH for 40 min to elute the template molecules, and the corresponding electrode was denoted as rMIP/$CdIn_2S_4@In_2S_3$/ITO. For comparison, the photoelectrode of NIP/$CdIn_2S_4@In_2S_3$/ITO was prepared by the same method in the absence of the CEA template.
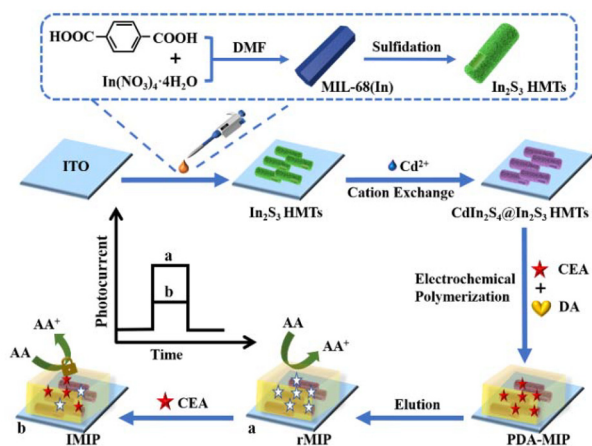
Scheme 1 Schematic of the preparation procedures for the $CdIn_2S_4@In_2S_3$ HMTs-based MIP-PEC sensor for CEA detection.

Photoelectrochemical measurements

Firstly, rMIP/CdIn$_2$S$_4$@In$_2$S$_3$/ITO was incubated for 40 min to capture the CEA molecules in 0.1 M PBS at pH 7.4 containing the different target concentrations, and the resulting photoanode was labeled as IMIP/CdIn$_2$S$_4$@In$_2$S$_3$/ITO. Subsequently, the photocurrent measurements were carried out in 0.1 M PBS at pH 7.4 containing 0.1 M AA with a bias voltage of 0 V. Similarly, PEC measurements of NIP/CdIn$_2$S$_4$@In$_2$S$_3$/ITO were performed by the same steps.

Results and discussion

Material characterizations

The morphologies and microstructures of the prepared materials were characterized using the SEM images. As shown in Fig. 1A, the MIL-68(In) precursor exhibited a smooth, hexagonal prism with a mean width of 1.06 μm. The In$_2$S$_3$ material could inherit the prism characteristics of MIL-68(In) after a simple sulphuration process, and exhibited a distinct hollow microtube with lots of nanosheet-based porous structures on the surface (Fig. 1B). After the Cd^{2+}-mediated, ion-exchange reaction, the nanosheets of CdIn$_2$S$_4$@In$_2$S$_3$ HMTs partly fell out, and a more distinct porous structure can be observed in Fig. 1C, which can serve as a desirable building substrate for the subsequent assembly of MIP. When PDA-MIP was electropolymerized onto the CdIn$_2$S$_4$@In$_2$S$_3$/ITO surface (Fig. 1D), MIP/CdIn$_2$S$_4$@In$_2$S$_3$/ITO was covered by the aggregated particles with a slight width increment of CdIn$_2$S$_4$@In$_2$S$_3$ HMTs. The surface particle density of rMIP/CdIn$_2$S$_4$@In$_2$S$_3$/ITO was then reduced due to the removal of the CEA template molecules (Fig. 1E). However, the microtubular morphology of NIP/CdIn$_2$S$_4$@In$_2$S$_3$ on the ITO electrode was maintained without a significant change in width compared to that of the CdIn$_2$S$_4$@In$_2$S$_3$ HMTs, which might be related to the absence of the template molecules (Fig. 1F).

The crystal structures of the prepared materials were analyzed by XRD. It can be seen from Fig. S1A that the XRD pattern of MIL-68(In) was similar to that of the simulated MOF precursor, and the characteristic peaks were typical of crystal plane diffractions.[31] As shown in Fig. S1B, the crystal structure of the ITO electrode was consistent with the diffraction peaks of (222), (400), (440), and (622).[32] In the XRD pattern of In$_2$S$_3$ HMTs, three diffraction peaks appeared near 2θ values of 27.8°, 33.5°, and 48.1°, which belonged to the (311), (400), and (440) lattice planes of In$_2$S$_3$ (JCPDS 32-0456), respectively.[33] After the ion-exchange reaction, five diffraction peaks were observed at 27.8°, 33.5°, 48.1°, 66.34°, and 76.35°, respectively, corresponding to the (311), (511), (440), (731) and (751) crystal faces of CdIn$_2$S$_4$ (JCPDS 31-0229).[34] Moreover, the elemental compositions of In$_2$S$_3$/ITO and CdIn$_2$S$_4$@In$_2$S$_3$/ITO were studied by EDS. As shown in Fig. S1C, the EDS spectrum of In$_2$S$_3$/ITO showed the obvious characteristic peaks of the In and S elements (curve a), and the existence of the Si element mainly resulted from the utilization of the ITO substrate.[35] From the EDS spectrum of CdIn$_2$S$_4$@In$_2$S$_3$ HMTs, a new characteristic peak was observed (curve b), which was derived from the presence of the Cd element.

X-ray photoelectron spectroscopy (XPS) was employed to further investigate the surface valence and chemical composition of CdIn$_2$S$_4$@In$_2$S$_3$ HMTs. As displayed in Fig. 2A, the XPS survey measurement confirmed that the CdIn$_2$S$_4$@In$_2$S$_3$ hybrid contained the elements In, Cd, and S, and the corresponding compositional distributions are presented in the EDS elemental mappings (Fig. S2). For the high-resolution XPS spectrum of Cd 3d (Fig. 2B), the characteristic peaks at binding energies of 412.4 eV and 405.6 eV corresponded to Cd 3d$_{3/2}$ and Cd 3d$_{5/2}$, respectively, indicating the presence of Cd^{2+}.[36] Similarly, the characteristic peaks of In 3d$_{3/2}$ and In 3d$_{5/2}$ were found at 453.6 eV and 446.0 eV (Fig. 2C), respectively, which revealed that the In element existed in the form of In^{3+}.[37] Two characteristic peaks of S 2p$_{1/2}$ and S 2p$_{3/2}$ were recorded at 163.1 eV and 161.9 eV (Fig. 2D), which confirmed the existence of S^{2-} in CdIn$_2$S$_4$@In$_2$S$_3$ HMTs.[38]

The chemical bonds and functional groups of In$_2$S$_3$ HMTs, CdIn$_2$S$_4$@In$_2$S$_3$ HMTs, and MIP-capped CdIn$_2$S$_4$@In$_2$S$_3$ HMTs
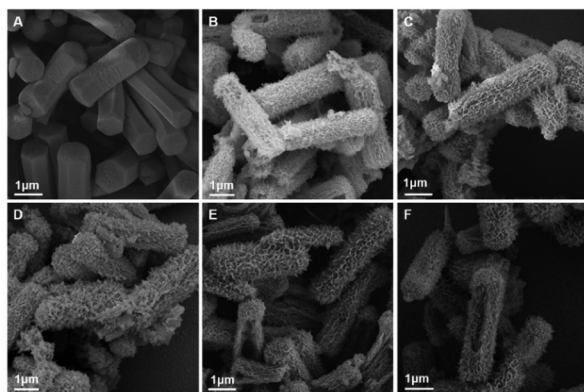
Fig. 1 SEM images of (A) MIL-68(In), (B) In$_2$S$_3$/ITO, (C) CdIn$_2$S$_4$@In$_2$S$_3$/ITO, (D) MIP/CdIn$_2$S$_4$@In$_2$S$_3$/ITO, (E) rMIP/CdIn$_2$S$_4$@In$_2$S$_3$/ITO and (F) NIP/CdIn$_2$S$_4$@In$_2$S$_3$/ITO.
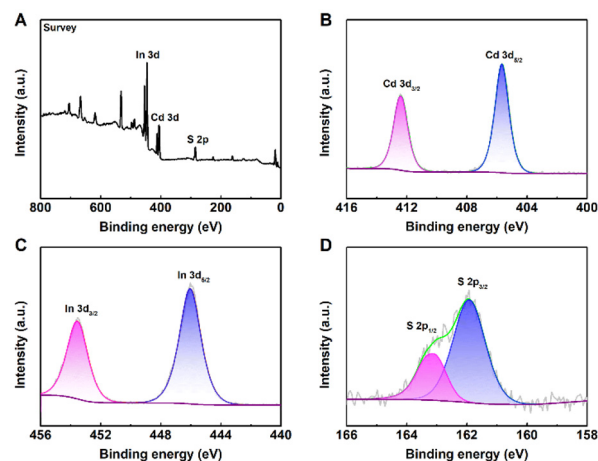

Fig. 2 XPS spectra of CdIn$_2$S$_4$@In$_2$S$_3$ HMTs: (A) survey, (B) Cd 3d, (C) In 3d, and (D) S 2p.

were identified by FT-IR spectroscopy (Fig. 3A). In the FT-IR spectrum of In_2S_3 (curve a), the strong characteristic bands located at 1028 cm^{-1} and 1630 cm^{-1} were assigned to the formation of the In_2S_3 composite, and the band at 3305 cm^{-1} corresponded to the –OH stretching vibrations because of the adsorbed water on the material's surface.[39–41] It should be noted that an enhancement of the peak intensity was observed at 1028 cm^{-1} in comparison to In_2S_3 HMTs (curve b), which indicated the presence of $CdIn_2S_4$ on the In_2S_3 surface.[42] After electropolymerization, three new bands appeared at 1612 cm^{-1}, 1468 cm^{-1}, and 3728 cm^{-1} (curve c), which corresponded to the N–H stretching, C=C stretching, and the phenolic O–H stretching vibrations in PDA.[43,44] UV–vis diffuse reflectance spectroscopy was utilized to investigate the visible absorption of the abovementioned materials (Fig. 3B). In comparison to In_2S_3 HMTs (curve a), $CdIn_2S_4@In_2S_3$ HMTs exhibited the higher absorption at 600 nm with a red-shifted band-edge position, and the increased absorption in the visible-light region was attributed to the heterostructure between $CdIn_2S_4$ and In_2S_3, which could accelerate the spatial separation of the electron–hole pairs. When PDA-MIP was electropolymerized onto $CdIn_2S_4@In_2S_3$ HMTs, MIP/$CdIn_2S_4@In_2S_3$ maintained a broad light-absorption region ranging from 330 nm to 800 nm because of the monotonous wavelength absorption of PDA,[45] ensuring a stable photocurrent.

Additionally, the bandgap of $CdIn_2S_4@In_2S_3$ HMTs (~2.16 eV, curve b) was narrower than that of In_2S_3 HMTs (~2.20 eV, curve a) according to the typical Kubelka–Munk theorem (Fig. S3A),[46] which further indicated the excellent visible-light absorption ability of $CdIn_2S_4/In_2S_3$ HMTs. The flat-band potentials of the prepared photoactive materials were then estimated from the Mott–Schottky plots. As shown in Fig. S3B, the flat-band potentials of In_2S_3 HMTs (curve a) and $CdIn_2S_4@In_2S_3$ HMTs (curve b) were −0.47 V and −0.40 V (vs. Ag/AgCl), respectively. Meanwhile, the positive slopes in the linear portion of Mott–Schottky plots were identified as the n-type semiconductors, and the type of $CdIn_2S_4@In_2S_3$ heterojunction belonged to a n–n junction.[47]

Feasibility of the MIP-PEC sensor

The recorded photocurrent responses of the layer-by-layer modified electrodes are shown in Fig. 4A. From this figure, the ITO electrode had almost no photocurrent signal (curve a),
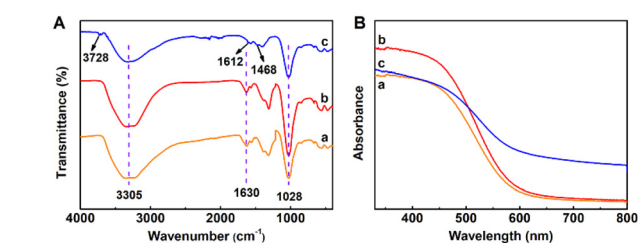

Fig. 3 (A) FT-IR and (B) UV–vis diffuse reflectance spectra of In_2S_3 HMTs (a), $CdIn_2S_4@In_2S_3$ HMTs (b), and MIP-capped $CdIn_2S_4@In_2S_3$ HMTs (c).
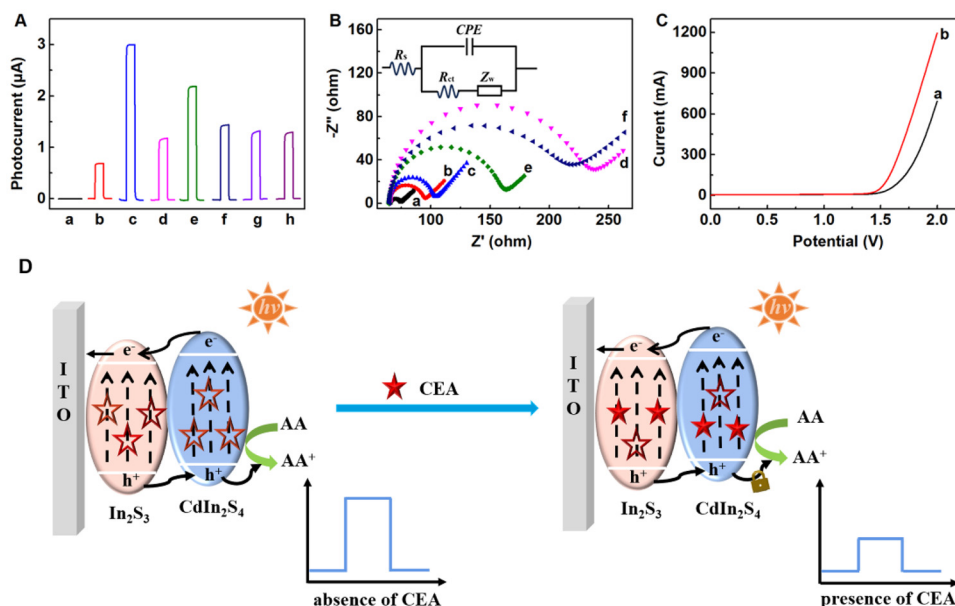
Fig. 4 (A) Photocurrent responses of the various modified electrodes: ITO (a), In_2S_3/ITO (b), $CdIn_2S_4@In_2S_3$/ITO (c), MIP/$CdIn_2S_4@In_2S_3$/ITO (d), rMIP/$CdIn_2S_4@In_2S_3$/ITO (e), IMIP/$CdIn_2S_4@In_2S_3$/ITO (f), NIP/$CdIn_2S_4@In_2S_3$/ITO (g), after the incubation of 100 ng mL^{-1} CEA (h). (B) EIS of the different electrodes: ITO (a), In_2S_3/ITO (b), $CdIn_2S_4@In_2S_3$/ITO (c), MIP/$CdIn_2S_4@In_2S_3$/ITO (d), rMIP/$CdIn_2S_4@In_2S_3$/ITO (e), and IMIP/$CdIn_2S_4@In_2S_3$/ITO (f). Target concentration was 100 ng mL^{-1}. Inset: the electrical equivalent circuit applied to the fit the impedance data; R_s, Z_w, R_{ct}, and CPE represent the Ohmic resistance of the electrolyte, Warburg impedance, charge-transfer resistance, and constant phase angle element, respectively. (C) Current–voltage tests of In_2S_3/ITO (a) and $CdIn_2S_4@In_2S_3$/ITO (b). Electrolyte: 0.1 M PBS at pH 7.4, scanning rate: 100 mV s^{-1}. (D) Photocurrent generation and regulation mechanisms of the designed MIP-PEC sensor.

and the photocurrent of In$_2$S$_3$/ITO was about 0.7 μA (curve b). After simple sulfidation, the formation of the CdIn$_2$S$_4$@In$_2$S$_3$ heterojunction could effectively promote the separation of the photoexcited charge carriers so that the photocurrent of CdIn$_2$S$_4$@In$_2$S$_3$/ITO largely increased to 3.0 μA (curve c). Obviously, the In$_2$S$_3$ HMTs served as the photoactive matrix and S^{2-} source for the subsequent assembly of CdIn$_2$S$_4$, which was beneficial for strengthening visible-light absorption and the detection signal of CdIn$_2$S$_4$@In$_2$S$_3$. When PDA-MIP was electropolymerized onto CdIn$_2$S$_4$@In$_2$S$_3$/ITO, the photocurrent of MIP/CdIn$_2$S$_4$@In$_2$S$_3$/ITO was reduced significantly due to the spatial barrier caused by the MIP coating (curve d). When the CEA template molecules were removed from MIP/CdIn$_2$S$_4$@In$_2$S$_3$/ITO, the exposed blotting cavities were beneficial for transferring the electron donor from the electrolyte to the photoactive material, leading to an enhancement of the photocurrent response (curve e). However, when the target, CEA, was incubated on the surface of rMIP/CdIn$_2$S$_4$@In$_2$S$_3$/ITO (curve f), a decrease in the photocurrent intensity occurred owing to a blockage of the CEA molecules assembled by rMIP. Contrastingly, the photocurrent of NIP/CdIn$_2$S$_4$@In$_2$S$_3$/ITO only changed slightly after the same preparation (curve g) and elution (curve h) processes, which indicated that NIP could not specifically recognize the CEA target.

The EIS measurements were also performed to investigate the preparation of the photoanodes under different steps, and the corresponding charge-transfer resistances (R_{ct}) were recorded by Nyquist plots.[48] As shown in Fig. 4B, the minimum R_{ct} value of the ITO electrode was only 66.1 Ω (curve a). When In$_2$S$_3$ (curve b) and CdIn$_2$S$_4$@In$_2$S$_3$ (curve c) were successively assembled onto the ITO electrode, the R_{ct} values increased to 73.4 Ω and 125.2 Ω, respectively, due to their poor conductivities,. After the electropolymerization reaction on CdIn$_2$S$_4$@In$_2$S$_3$/ITO (curve d), the value of R_{ct} increased to 237.3 Ω because of the introduction of PDA-MIP.[49,50] Subsequently, a sharp decline in the R_{ct} value was observed (curve e) because the cavities formed by CEA elution could provide the effective transfer channels for the electrochemical probe. However, the R_{ct} value increased again when the cavities of rMIP were re-embedded by target CEA (curve f).

Moreover, current–voltage measurements were carried out in the potential range of 0 V to 2.0 V. As shown in Fig. 4C, the current of CdIn$_2$S$_4$@In$_2$S$_3$/ITO increased rapidly and was larger than that of In$_2$S$_3$/ITO when the applied voltage was greater than 1.5 V, which was attributed to the construction of the CdIn$_2$S$_4$@In$_2$S$_3$ heterojunction.[51] The possible electron transfer pathway is described as follows (Fig. 4D): Under light irradiation, CdIn$_2$S$_4$ and In$_2$S$_3$ were excited to produce electron–hole pairs, in which the photogenerated electrons were transferred from the conduction band (CB) of CdIn$_2$S$_4$ to that of In$_2$S$_3$, and then transported to the ITO electrode. Meanwhile, the photogenerated holes were transferred from the valence band (VB) of In$_2$S$_3$ to that of CdIn$_2$S$_4$, and then captured by the electron donor, preventing the recombination of the electron–hole pairs, resulting in a stable photocurrent.[52] When the target molecules were added onto rMIP/

CdIn$_2$S$_4$@In$_2$S$_3$/ITO, the imprinted cavities could be re-occupied, thereby hindering the diffusion and electron transfer between the electron donor and photoactive material and resulting in the reduction of the photocurrent intensity.

Optimization of experimental conditions

To achieve MIP-PEC with excellent properties, several experimental parameters, such as the concentration of the CEA template, the number of electrochemical polymerization cycles, the elution time for the CEA template, and the incubation time between the CEA target and rMIP, were systematically investigated (Fig. S4). Among these parameters, several trends in the photocurrent change ($\Delta I = I_0 - I$) were measured, where I_0 and I were the photocurrent of the MIP-PEC sensor incubated in the detection solution without and with CEA, respectively. As shown in Fig. S4A, the photocurrent of the MIP-PEC sensor increased with the increasing concentration of the CEA template in the range of 0.1 μg mL^{-1} to 0.5 μg mL^{-1}, and then decreased with a further increase in the CEA concentration; hence, 0.5 μg mL^{-1} was selected as the optimal template concentration. Similarly, the effect of the electropolymerization cycles on the MIP-PEC sensor was examined (Fig. S4B). The maximum change in the ΔI value was observed at 20 cycles. Thus, 20 cycles were chosen for the DA-based polymerization reaction.

The elution time was also studied as an important factor of the sensing proprieties. As shown in Fig. S4C, the ΔI value of the MIP-PEC sensor varied with the elution time, and reached a maximum value at 40 min. After that value, the photocurrent basically remained unchanged despite the extension of time. Therefore, 40 min was the optimal elution time. Furthermore, it can be seen from Fig. S4D that when the photocurrent changes of the MIP-PEC sensor increased to 40 min, a plateau was achieved with any further extension of the incubation time because adsorption equilibrium between CEA and rMIP was reached. Thus, 40 min was taken as the optimal incubation time.

Analytical performances of the developed sensor

The properties of the constructed MIP-PEC sensor were investigated after it was incubated with different concentrations of the CEA samples. As depicted in Fig. 5A, a gradual declining
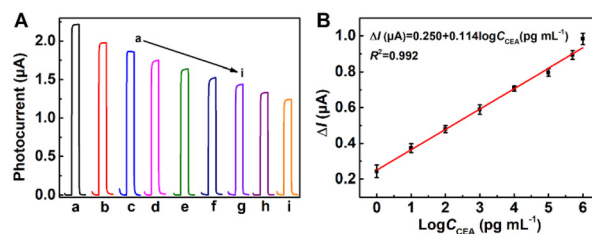

Fig. 5 (A) Photocurrent responses of the designed sensor under different concentrations of the CEA target: 0 (a), 1 (b), 10 (c), 100 (d), 1000 (e), 10 000 (f), 100 000 (g), 500 000 (h), 1 000 000 (i) pg mL^{-1}. (B) The corresponding calibration curves.

trend in the photocurrent was observed with the incremental increase in the CEA level because the adsorbed CEA molecules in the imprinted cavities effectively hindered diffusion and electron transfer from the electron donor to the photoactive material. Meanwhile, a linear relationship between the photocurrent intensity and the logarithm of CEA concentration was obtained in the range of 1 pg mL^{-1} to 500 ng mL^{-1}, and the linear regression equation was ΔI (μA) = 0.250 + 0.114 log C_{CEA} (pg mL^{-1}) with a correlation coefficient of R^2 = 0.992 (Fig. 5B). The limit of detection (LOD) was determined to be 0.52 pg mL^{-1} at 3σ. Moreover, the performance comparisons between the above MIP-PEC sensor and other previously reported CEA sensors/biosensors are summarized in Table S1. Obviously, the designed MIP-PEC sensor can achieve comparable or superior abilities within the linear range and detection limit due to the desirable photo-to-current conversion of CdIn$_2$S$_4$@In$_2$S$_3$ HMTs and the specific binding sites of rMIP.

The stability of the constructed MIP-PEC sensor was examined in Fig. 6A. It can be seen from this figure that no distinct photocurrent change was observed after continuous "on–off" light irradiation for 18 cycles; this shows that the sensor has excellent cycling stability. When the photoanodes were stored for 1 and 2 weeks at 4 °C, the detection signal maintained 96.8% and 93.2% of the original value, respectively. In addition, five independent measurements of the MIP-PEC sensors were performed with 100 ng mL^{-1} CEA, and the relative standard deviation (RSD) was 2.68%. Thus, the proposed MIP-PEC sensor had good long-term stability and acceptable reproducibility for the CEA assay.

Furthermore, several potential biomarkers, such as alpha-fetoprotein antigen (AFP), prostate-specific antigen (PSA), thrombin (TB), and their mixtures, were detected for assessing the specificity of MIP-PEC sensor. As shown in Fig. 6B, the change in the photocurrent of the sensor for the target sample was 0.8 μA, which was approximately 3.8, 4.7 and 4.4 times that of the sensor for the AFP, PSA, and TB samples, respectively. However, the ΔI value for the mixed sample indicated only a slight photocurrent change in comparison to that for the CEA sample. Obviously, the specific shape and size of the blotting cavities in rMIP can enable selective binding to target molecules by means of a complementary spatial configuration
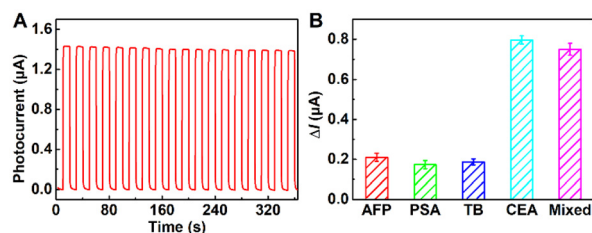
Table 1 Comparison of the proposed and reference methods for the CEA assay in human serum samples (n = 5)

Samples	Reference method (ng mL^{-1})	Proposed method (ng mL^{-1})	RSD
1	0.50	0.47	7.02%
2	1.36	1.33	2.93%
3	4.47	4.41	1.11%

and hydrogen-bond interaction. Thus, the above sensor had excellent anti-interference ability due to the introduction of PDA-MIP.

CEA analysis in human serum samples

The practicality of the developed MIP-PEC sensor was also investigated. All the human serum samples used were available from Subei People's Hospital in Yangzhou City. Prior to CEA testing, the serum samples were diluted with 0.01 M PBS at pH 7.4 to avoid the influence of a high tissue level on target recognition. As shown in Table 1, the detection results of the proposed sensor were 0.47, 1.33, and 4.41 ng mL^{-1}, respectively, which had no distinct change compared to the corresponding values from the reference electrochemiluminescence method (e.g., 0.50, 1.36, and 4.47 ng mL^{-1}), and the related RSD values were no more than 7.02%, indicating great potential for clinical diagnostic applications.

Conclusions

In summary, an antibody-free molecularly imprinted PEC sensor was developed for the CEA assay based on CdIn$_2$S$_4$@In$_2$S$_3$ HMTs and PDA-MIP. Among the synthesised compounds, the heterostructured CdIn$_2$S$_4$@In$_2$S$_3$ had excellent photoelectric properties under visible-light excitation. When the template molecules were eluted from PDA-MIP, abundant cavities were formed that specifically recognized the target, CEA, due to the high binding interaction between the target molecules and rMIP, which effectively improved the selectivity of the sensing platform. Under optimal conditions, this MIP-PEC sensor exhibited a wide linear range of 0.001–500 ng mL^{-1}, low detection limit of 0.52 pg mL^{-1}, and good stability, and was applied to the CEA assay in human serum, providing a feasible strategy for the sensitive and selective detection of other disease markers.

Author contributions

Yang Zang: conceptualization, writing – review & editing, formal analysis, methodology, resources, supervision, funding acquisition. Ruhua Wei: material synthesis, data curation, validation, writing – original draft, writing – review & editing, visualization, formal analysis. Yang Feng: formal analysis. Jingjing Jiang: conceptualization, formal analysis, funding acquisition. Huaiguo Xue: resources, project administration.

Fig. 6 (A) Time-based photocurrent response of the proposed sensor under continuous "off–on–off" irradiation. (B) Selectivity of the designed sensor for the CEA target in comparison to other interfering substances at 100 ng mL^{-1}: AFP, PSA, TB, CEA, and the mixture containing AFP, PSA, TB and CEA.

Conflicts of interest

There are no conflicts of interest to declare.

Data availability

Acknowledgements

References

1 L. R. Li, Y. R. Bo, P. Miao, J. Chang, Y. Zhang, B. Y. Ding, Y. F. Lv, X. F. Yang, J. Zhang and M. Yan, *Biosens. Bioelectron.*, 2024, **250**, 116075.

2 M. Hadian, M. Rabbani, L. Shariati, F. Ghasemi, J. F. Presley and A. Sanati, *ACS Sens.*, 2025, **10**, 857–867.

3 S. Agrahari, A. K. Singh, I. Tiwari and S. Srikrishna, *Microchem. J.*, 2024, **196**, 109698.

4 Y. L. Sun, Y. N. Hou, T. Z. Cao, C. N. Luo and Q. Wei, *Anal. Chem.*, 2023, **95**, 7387–7395.

5 Y. Zang, R. Cao, C. Y. Zhang, Q. Xu, Z. J. Yang, H. G. Xue and Y. Z. Shen, *Biosens. Bioelectron.*, 2021, **185**, 113251.

6 S. M. Wang, X. Y. Li, X. L. Wang, X. D. Wu, D. G. Jiang, H. Zhou, S. X. Gao and J. Liu, *Biosens. Bioelectron.*, 2024, **253**, 116170.

7 H. F. Shen, C. Wang, C. L. Ren, G. S. Zhang, Y. C. Zhang, J. Li, X. Y. Hu and Z. J. Yang, *New J. Chem.*, 2020, **44**, 6010–6014.

8 Q. Z. Han, N. Na and J. Ouyang, *Anal. Chim. Acta*, 2024, **1292**, 342222.

9 G. Liu, H. Gao, J. J. Chen, C. Y. Shao and F. F. Chen, *Electroanalysis*, 2021, **33**, 1444–1450.

10 Z. X. Zhong, L. Ding, Z. Man, Y. A. Zeng, B. C. Pan, J. J. Zhu, M. Zhang and F. L. Cheng, *Anal. Chem.*, 2024, **96**, 8837–8843.

11 C. F. Wang, Y. Tang, B. H. Zhang, Z. Y. Zhong, F. Q. Zhao and B. Z. Zeng, *Anal. Chim. Acta*, 2023, **1262**, 341243.

12 F. Mo, M. Han, X. Weng, Y. Y. Zhang, J. Li and H. B. Li, *Anal. Chem.*, 2021, **93**, 1764–1770.

13 L. X. Meng, Q. Q. Wu, J. L. Wang, B. X. Zhou, J. J. Shi and K. Xiao, *Electrochim. Acta*, 2025, **529**, 146341.

14 Y. H. Pi, S. Jin, X. Y. Li, S. Tu, Z. Li and J. Xiao, *Appl. Catal., B*, 2019, **256**, 117882.

15 H. B. Chen, Y. J. Xing, S. C. Liu, Y. J. Liang, J. L. Fu, L. J. Wang and W. Z. Wang, *Chem. Eng. J.*, 2023, **462**, 142038.

16 J. Zhang, L. Zhao, Y. D. Xue, A. J. Wang, L. P. Mei, P. Song and J. J. Feng, *Microchim. Acta*, 2025, **192**, 144.

17 L. F. Yang, A. Q. Li, T. Dang, Y. F. Wang, L. Liang, J. Tang, Y. J. Cui and Z. Z. Zhang, *Appl. Surf. Sci.*, 2023, **612**, 155848.

18 F. F. You, T. H. Zhou, J. X. Li, S. H. Huang, C. T. Chang, X. Y. Fan, H. Zhang, X. H. Ma, D. W. Gao, J. Qi and D. Y. Li, *J. Colloid Interface Sci.*, 2024, **660**, 77–86.

19 J. J. Peng, J. Y. Yang, B. Chen, S. S. Zeng, D. L. Zheng, Y. W. Chen and W. H. Gao, *Biosens. Bioelectron.*, 2021, **175**, 112873.

20 Q. Y. Wang, L. H. Wang, Y. H. Jiang, Y. Liu, W. L. Zhang, J. M. Zhang and A. L. O. Macauley, *Environ. Res.*, 2022, **209**, 112800.

21 Y. A. Lu, H. L. Liu, L. Wang, Y. L. Geng and M. M. Zhang, *J. Alloys Compd.*, 2024, **982**, 173750.

22 Y. Q. Chen, Y. F. Cheng, J. F. Zhao, W. W. Zhang, J. H. Gao, H. Miao and X. Y. Hu, *J. Colloid Interface Sci.*, 2022, **627**, 1047–1060.

23 R. Bariki, D. Majhi, K. Das, A. Behera and B. G. Mishra, *Appl. Catal., B.*, 2020, **270**, 118882.

24 J. H. Zhu, M. Wang, L. H. Tu, A. J. Wang, X. L. Luo, L. P. Mei, T. J. Zhao and J. J. Feng, *Sens. Actuators, B*, 2021, **347**, 130553.

25 X. Q. Wang, H. Y. Chen, J. H. Zhang, H. Zhou, X. Y. Meng, N. Wang, Y. S. Feng and B. Cui, *Food Chem.*, 2024, **441**, 138299.

26 Y. A. Zeng, M. Zhang, K. F. Peng, Z. Man, L. A. Guo, W. P. Liu, S. L. Xie, P. Liu, D. Xie, S. S. Wang and F. L. Cheng, *Microchim. Acta*, 2023, **190**, 244.

27 C. Y. Wang, Y. Y. Wang, H. J. Zhang, H. P. Deng, X. X. Xiong, C. Y. Li and W. W. Li, *Anal. Chim. Acta*, 2019, **1090**, 64–71.

28 Y. Zang, Y. Zhang, R. H. Wei, H. G. Xue and J. J. Jiang, *J. Electroanal. Chem.*, 2023, **944**, 117631.

29 Z. T. Yang, J. Q. Wang, T. Shah, P. Liu, M. Ahmad, Q. Y. Zhang and B. L. Zhang, *Talanta*, 2021, **224**, 121760.

30 S. C. Zhao, K. Y. Li, J. Du, C. S. Song and X. W. Guo, *ACS Sustainable Chem. Eng.*, 2021, **9**, 5942–5951.

31 X. Huang, Q. Y. Lin, L. L. Lu, M. J. Li and D. P. Tang, *Anal. Chim. Acta*, 2022, **1228**, 340358.

32 S. M. Yang, B. S. Sun, Y. Liu, J. P. Zhu, J. X. Song, Z. H. Hao, X. Y. Zeng, X. Zhao, Y. C. Shu, J. Chen, J. H. Yi and J. L. He, *Ceram. Int.*, 2020, **46**, 6342–6350.

33 R. Souissi, N. Bouguila, B. Bouricha, C. Vázquez-Vázquez, M. Bendahan and A. Labidi, *RSC Adv.*, 2020, **10**, 18841–18852.

34 T. T. Wu, J. H. Feng, S. T. Zhang, L. Liu, X. Ren, D. W. Fan, X. Kuang, X. Sun, Q. Wei and H. X. Ju, *Biosens. Bioelectron.*, 2020, **169**, 112580.

35 R. Souissi, N. Bouguila, M. Bendahan, K. Aguir, T. Fiorido, M. Abderrabba, I. Halidou and A. Labidi, *J. Alloys Compd.*, 2022, **900**, 163513.

36 L. Gao, Z. Chen, H. Zheng and J. Hu, *Mater. Today Chem.*, 2022, **24**, 100800.

37 X. H. Zhao, Y. T. Zhou, Q. Liang, M. Zhou, Z. Y. Li and S. Xu, *Sep. Purif. Technol.*, 2021, **279**, 119765.

38 J. J. Wei, H. B. Li, G. Q. Wang, J. Y. Zheng, A. J. Wang, L. P. Mei, T. J. Zhao and J. J. Feng, *Anal. Chem.*, 2022, **94**, 12240–12247.

39 X. Z. Yuan, L. B. Jiang, J. Liang, Y. Pan, J. Zhang, H. Wang, L. J. Leng, Z. B. Wu, R. P. Guan and G. M. Zeng, *Chem. Eng. J.*, 2019, **356**, 371–381.

40 J. Fan, Y. Zang, J. J. Jiang, J. P. Lei and H. G. Xue, *Biosens. Bioelectron.*, 2019, **142**, 111557.

41 P. Zhang, X. Yin, D. G. Zhang, P. Y. Guo, W. B. Liu, R. W. Wang, Z. T. Zhang and S. L. Qiu, *Chem. Eng. J.*, 2023, **458**, 141394.

42 S. Z. Alsheheri and R. M. Mohamed, *Opt. Mater.*, 2021, **123**, 111946.

43 S. Palanisamy, B. Thirumalraj, S. M. Chen, Y. T. Wang, V. Velusamy and S. K. Ramaraj, *Sci. Rep.*, 2016, **6**, 33599.

44 Y. Z. Shen, W. Z. Xie, Z. Wang, K. P. Ning, Z. P. Ji, H. B. Li, X. Y. Hu, C. Ma and Q. Xu, *Biosens. Bioelectron.*, 2024, **254**, 116201.

45 B. W. Gao, Z. S. Liang, D. X. Han, F. J. Han, W. C. Fu, W. Wang, Z. B. Liu and L. Niu, *Talanta*, 2021, **224**, 121924.

46 H. Y. Wang, J. Tang, X. Y. Wan, X. Wang, Y. Y. Zeng, X. L. Liu and D. P. Tang, *Anal. Chem.*, 2024, **96**, 15503–15510.

47 J. H. Zheng and Z. Lei, *Appl. Catal., B*, 2018, **237**, 1–8.

48 J. N. Chen, G. K. Hasabnis, E. Akin, G. Y. Gao, S. P. Usha, R. Süssmuth and Z. Altintasa, *Sens. Actuators, B*, 2024, **417**, 136052.

49 Y. H. He, J. Sun, W. Q. Yao, K. N. Lu, D. Q. Liu, H. J. Xie, C. S. Huang and N. Q. Jia, *Chem. Eng. J.*, 2023, **451**, 138748.

50 C. Li, D. F. Han, Z. F. Wu, Z. S. Liang, F. J. Han, K. Chen, W. C. Fu, D. X. Han, Y. K. Wang and L. Niu, *Analyst*, 2022, **147**, 3291–3297.

51 Y. Zang, J. Fan, H. Zhang, Q. Xu, J. J. Jiang and H. G. Xue, *Electrochim. Acta*, 2020, **334**, 135581.

52 Y. X. Li, L. Li, X. Y. Dong, Z. C. Xin, J. H. Guan, X. Y. Gao, W. L. Zu and W. Z. Zhang, *J. Alloys Compd.*, 2022, **909**, 164701.